

Supplementary Information: Transport signatures of relativistic quantum scars in a graphene cavity

G. Q. Zhang,^{1,*} Xianzhang Chen,^{2,*} Li Lin,³ Hailin Peng,³ Zhongfan Liu,³ Liang Huang,^{2,†} N. Kang,^{1,‡} and H. Q. Xu^{1,4,§}

¹*Beijing Key Laboratory of Quantum Devices, Key Laboratory for the Physics and Chemistry of Nanodevices and Department of Electronics, Peking University, Beijing 100871, P. R. China*

²*School of Physical Science and Technology and Key Laboratory for Magnetism and Magnetic Materials of MOE, Lanzhou University, Lanzhou, Gansu 730000, P. R. China*

³*Center for Nanochemistry, Beijing Science and Engineering Center for Nanocarbons, Beijing National Laboratory for Molecular Sciences, College of Chemistry and Molecular Engineering, Peking University, Beijing 100871, P. R. China*

⁴*Beijing Academy of Quantum Information Sciences, Beijing 100193, China*

I. MODEL

In the theoretical calculations, the graphene cavity device studied experimentally in the main article was modeled by a lattice structure as shown in Fig. S1 within the framework of a tight-binding Hamiltonian with hopping integrals of up to the third-nearest neighbors included [1–3]. Restricted by the limitation of our computation power, modeling of the cavity device with its actual size of $D \sim 1 \mu\text{m}$ is not feasible. However, the transport properties of a large graphene system can be characterized by a model system of a smaller dimension if the Fermi energy and the magnetic field are scaled to appropriate ranges [4]. With increasing magnetic field B applied perpendicularly to the graphene plane, the classic cyclotron radius of the charge carrier decreases as $R = \hbar k_F/eB$ [5], where \hbar is the reduced Planck constant, k_F is the Fermi wave vector and e is the elementary charge. Once the magnetic field goes beyond a maximum value of $B_{\max} = \hbar k_F/eD$, R reaches the cavity dimension D , and then edge states begin to form and the quantum Hall effect dominates. This quantum Hall regime is beyond our modeling, since our focus is on the range where the magnetic field is lower than B_{\max} . As the model is scaled down in dimension from the experimental value D to a smaller one D_{scale} , the corresponding investigated magnetic fields can be extended to $B_{\text{scale}} = \hbar k_F/eD_{\text{scale}}$ without going into the quantum Hall regime. As the schematic model displayed in Fig. S1, we have scaled the cavity device to a smaller size of 19.2 nm in height (the distance between the upper and lower cavity boundaries) and 16 nm in width (the distance between the two narrow constrictions). Thus, the magnetic fields employed in the calculations can be scaled up to ~ 50 times larger without making the model system into the quantum Hall regime. In the calculations, the considered magnetic fields are set to the range of -30 T to 30 T. One may employ the scaling relation given in Ref. 4, $D = \frac{2\hbar(E/t)}{3\sqrt{3}ea_0B}$, where E is the Fermi energy, $t(\approx 2.8 \text{ eV})$ is the nearest neighbor hopping energy [5], and $a_0 = 0.142 \text{ nm}$ is the distance between two nearest-neighbor atoms of graphene, to scale the magnet-

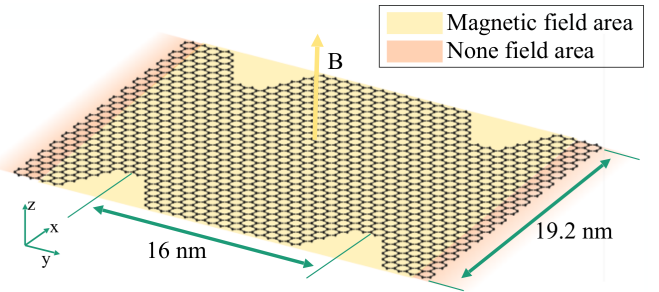


FIG. S1: Schematic illustration of the graphene cavity device used in the calculations in a perpendicular magnetic field. Note that the magnetic field exists only in the device region.

ic field and Fermi energy considered in the model calculations to the corresponding values in the measured cavity device.

II. COMPUTATION METHOD

To understand the measured transport characteristics of the graphene cavity device, we have performed the calculations for the conductance as a function of the magnetic field applied perpendicularly to the graphene sheet and the Fermi energy (conductance map) of the model device, and for the wave function probability distributions and current density distributions at a few representative points selected from the conductance map. The conductance is calculated via the Landauer formalism which relates the two-terminal conductance G of the device to the transmission coefficient T [6] via

$$G(E_F) = \frac{2e^2}{h} T_G(E_F), \quad (1)$$

with

$$T_G(E_F) = \int T(E) \left(-\frac{\partial f}{\partial E} \right) dE,$$

where $T(E)$ is the transmission of the device and $f(E) = 1/[1 + e^{(E-E_F)/kT}]$ is the Fermi distribution function. At low temperature, $-\partial f/\partial E \approx \delta(E - E_F)$, thus $T_G(E_F) = T(E_F)$ and $G(E_F) = (2e^2/h)T(E_F)$. In this work, we focus on the study of the low-temperature conductance, or equivalently, the low-temperature transmission T .

*These authors contributed equally to this work.

†Corresponding author: huangl@lzu.edu.cn

‡Corresponding author: nkang@pku.edu.cn

§Corresponding author: hqxu@pku.edu.cn

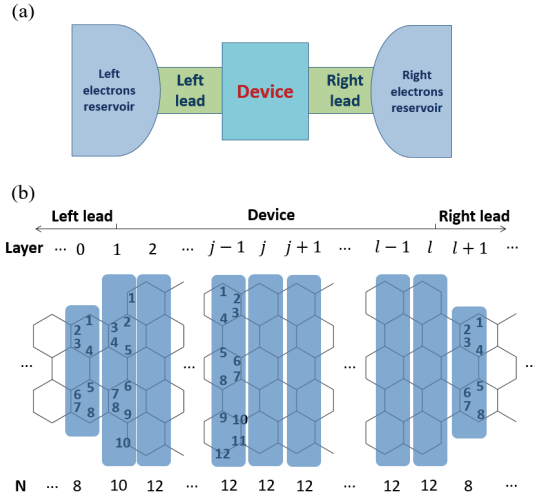


FIG. S2: (a) Schematic illustration of a device with leads and reservoirs. (b) Illustration of construction of tight-binding Hamiltonian for calculating Green's function. The device consists of layer 1 to layer l . The left lead is from layer $-\infty$ to layer 0 and the right lead is from layer $l+1$ to layer ∞ . The numbers in the bottom of the figure indicate the number of atoms in each layer.

We employ the Green's function formalism [7, 8] to calculate the transmission $T(E)$ for the model graphene cavity. The tight-binding Hamiltonian for electrons in graphene including the hopping terms up to the third-nearest-neighbor atoms takes the form [1–3],

$$\hat{H} = -t \sum_{i,j \in \text{n.n.}} e^{-i\phi_{ij}} c_i^+ c_j - t' \sum_{i,j \in \text{n.n.n.}} e^{-i\phi_{ij}} c_i^+ c_j - t'' \sum_{i,j \in \text{t.n.n.}} e^{-i\phi_{ij}} c_i^+ c_j, \quad (2)$$

where t, t', t'' represent the nearest-neighbor (n.n.), next-nearest-neighbor (n.n.n.) and third-nearest-neighbor (t.n.n.) hopping energies, which take the values of 2.8 eV, 0.28 eV and 0.07 eV [1–3], respectively, and $\phi_{ij} = (2\pi/\phi_0) \int_{r_j}^{r_i} d\mathbf{r} \cdot \mathbf{A}$, where $\phi_0 = h/e$ is the magnetic flux quantum, \mathbf{A} is the vector potential associated with the applied magnetic field. Using the Landau gauge, the vector potential is given by $\mathbf{A} = (By, 0, 0)$ for a perpendicular uniform magnetic field \mathbf{B} pointing out of the cavity plane. The magnetic field is applied only in the device region in our simulation. Note that the Dirac point will be shifted to $3t'$ when considering the next-nearest-neighbor hopping energy [1, 9].

In general, the device is regarded as a scattering region and links two large ideal electrons reservoirs through the left and right leads [Fig. S2(a)]. In our model, the leads are assumed to be semi-infinite to eliminate spurious reflections, and the system can be divided into three parts: left lead, device, and right lead. The device is chosen to include all irregular parts so that the left and the right leads are uniform in width. Under

these assumptions, the Hamiltonian can be written in a matrix form,

$$H = \begin{pmatrix} H_L & H_{LD} & 0 \\ H_{DL} & H_D & H_{DR} \\ 0 & H_{RD} & H_R \end{pmatrix}. \quad (3)$$

In the above Hamiltonian, H_D is a finite-size square matrix of dimension $N_D \times N_D$, where N_D is the number of atoms in the device, and $H_{L,R}$ are the Hamiltonians of the left lead and right lead, respectively. The couplings between the device and the leads are given by the matrices H_{LD}, H_{DL}, H_{DR} , and H_{RD} .

Using layer indices as subscripts, the Hamiltonian can be written in terms of layer Hamiltonians. For example, for the device shown in Fig. S2(b), we have

$$H_D = \begin{pmatrix} H_{11} & H_{12} & 0 & 0 & 0 \\ H_{21} & H_{22} & H_{23} & 0 & 0 \\ 0 & \dots & \ddots & \dots & 0 \\ 0 & H_{j-1,j-2} & H_{j-1,j-1} & H_{j,j-1} & 0 \\ 0 & H_{j,j-1} & H_{j,j} & H_{j+1,j} & 0 \\ 0 & H_{j+1,j} & H_{j+1,j+1} & H_{j+2,j+1} & 0 \\ 0 & \dots & \ddots & \dots & 0 \\ 0 & 0 & H_{l-1,l-2} & H_{l-1,l-1} & H_{l-1,l} \\ 0 & 0 & 0 & H_{l,l-1} & H_{l,l} \end{pmatrix},$$

where, for instance, H_{11} is the Hamiltonian matrix for layer 1, whose size is $N_1 \times N_1 = 10 \times 10$, and H_{01} is the coupling matrix from layer 1 to layer 0, which has a size of $N_0 \times N_1 = 8 \times 10$. Note that $H_{00} = H_{-1,-1} = H_{-2,-2} = \dots = H_{l+1,l+1} = H_{l+2,l+2} = \dots$. In the Hamiltonian, t is the only parameter (t' and t'' can be written in units of t). Thus, in the calculations for transmission T , it is convenient to use t as the energy unit.

The Green's function $G(E)$ is defined by

$$(E^\dagger I - H)G(E) = I, \quad (4)$$

where I is the identity matrix, $E^\dagger = E + i\eta$ with $(\eta \rightarrow 0^+)$. Thus, $G(E) = (E^\dagger I - H)^{-1}$. Here we should note that G and H are the Green's function and the Hamiltonian of the whole system, and are infinite in size. The Green's function of the device after including the effects due to coupling to the leads is given by

$$G_D(E) = (E^\dagger I - H_D - \Sigma_L - \Sigma_R)^{-1}, \quad (5)$$

where Σ_L and Σ_R are the self-energies arising from the couplings to the left and to the right lead, respectively,

$$\begin{aligned} \Sigma_L &\equiv H_{DL} G_L H_{LD}, \\ \Sigma_R &\equiv H_{DR} G_R H_{RD}, \end{aligned}$$

with $G_{L,R}$ being the Green's functions of the left and the right lead. Note that the self-energies add nonzero elements only on the atoms in the device adjacent to the leads [10], i.e.,

$$\Sigma_L = \begin{pmatrix} \Sigma_{L,1} & 0 \\ 0 & 0 \end{pmatrix}, \Sigma_R = \begin{pmatrix} 0 & 0 \\ 0 & \Sigma_{R,l} \end{pmatrix},$$

where $\Sigma_{L,l}$ and $\Sigma_{R,l}$ correspond to the self-energies of layer 1 and layer l , respectively, and can be calculated using a standard procedure [8, 11].

Now, all the matrices in Eq. (5) are in a size of $N_D \times N_D$, where N_D is the size (number of atoms) of the device. The coupling matrices $\Gamma_{L,R}$ between the left/right lead and the device are the differences between the corresponding retarded and advanced self-energies:

$$\Gamma_{L,R} = i[\Sigma_{L,R} - (\Sigma_{L,R})^\dagger].$$

The transmission of the system is then

$$T(E) = \text{Tr}(\Gamma_L G_D \Gamma_R G_D^\dagger). \quad (6)$$

The local density of states (LDOS, an N_D dimensional vector) for the device is

$$\rho = -\frac{1}{\pi} \text{Im}[\text{diag}(G_D)]. \quad (7)$$

In the tight-binding approach, the elements of the LDOS vector give the wave function probability distribution in the device region.

The current density distribution can be obtained from the local current flows between neighboring lattice points i and j via [12]

$$J_{i \rightarrow j} = \frac{4e}{h} \text{Im}[H_{D,ij} C_{ji}^n(E)], \quad (8)$$

where $C^n = G_D \Gamma^L G_D^\dagger$ is the electron correlation function and $H_{D,ij}$ is the Hamiltonian matrix element.

Although the physical picture of the above scheme is clear, the computation efficiency is low as it employs many inversion operations of $N_D \times N_D$ matrices. Therefore, an efficient recursive method is employed in the calculation for this work. In particular, it can be noticed that each layer j can be regarded as the “device”, while the rest layers can be regarded as non-uniform leads. To be specific, for layer 1, since its self-energy from left leads $\Sigma_{L,1}$ is known, following the iterative relation,

$$\Sigma_{L,j+1} = H_{j+1,j} (E^\dagger I - H_{j,j} - \Sigma_{L,j})^{-1} H_{j,j+1},$$

the self-energy due to the coupling to the lattices on the left side, $\Sigma_{L,j}$, for every layer j can be calculated. Similarly, since $\Sigma_{R,l}$ is known, following

$$\Sigma_{R,j-1} = H_{j-1,j} (E^\dagger I - H_{j,j} - \Sigma_{L,j})^{-1} H_{j,j-1},$$

the self-energy due to coupling to the lattices on the right lead, $\Sigma_{R,j}$, for every layer j can also be calculated. Thus, for each layer j , the self-energies due to couplings to both the left and the right side, $\Sigma_{L,j}$ and $\Sigma_{R,j}$, are known. Then, similar to Eq. (5), the complete Green’s function for this layer (regarding this layer as the device) can be calculated,

$$G_j(E) = (E^\dagger I - H_{j,j} - \Sigma_{L,j} - \Sigma_{R,j})^{-1}. \quad (9)$$

The coupling matrices are:

$$\begin{aligned} \Gamma_{L,j} &= i[\Sigma_{L,j} - (\Sigma_{L,j})^\dagger], \\ \Gamma_{R,j} &= i[\Sigma_{R,j} - (\Sigma_{R,j})^\dagger]. \end{aligned}$$

The transmission is then

$$T_j(E) = \text{Tr}(\Gamma_{L,j} G_j \Gamma_{R,j} G_j^\dagger). \quad (10)$$

The wave function probability distribution (LDOS vector) in the layer j is given by

$$\rho_j = -\frac{1}{\pi} \text{Im}[\text{diag}(G_j)]. \quad (11)$$

The current density distribution is obtained from [12]

$$J_{i \rightarrow k} = \frac{4e}{h} \text{Im}[H_{jj,ik} C_{j,ki}^n(E)], \quad (12)$$

where $C_j^n = G_j \Gamma^L G_j^\dagger$ is the electron correlation function and $H_{jj,ki}$ is the Hamiltonian matrix element with indices i and k .

III. CONDUCTANCE MAPS OF GRAPHENE CAVITIES OF DIFFERENT SIZES

Here we provide numerical evidence that the conductance maps of graphene cavities of different sizes exhibit similar features if the ranges of Fermi energy and magnetic field are scaled properly.

Figure S3 shows the calculated conductance as a function of Fermi energy and magnetic field (conductance maps) for three graphene cavities of the same shapes but different sizes. More specifically, the shapes of the devices considered in Figs. S3(a), S3(b) and S3(c) are the same shape, but the widths of the cavities in the devices are 11.5 nm, 15.3 nm and 19.2 nm, respectively. It is clearly seen that the conductance maps of the three devices exhibit common features of straight and parabolic high conductance contour lines, although exact one-to-one correspondences between them can not be expected. Therefore, one can use a smaller model system to demonstrate and explain the high conductance contour features observed experimentally in a large graphene cavity device.

IV. DISCUSSION ON THE UNDERLYING PHYSICS OF THE CHARACTERISTIC HIGH CONDUCTANCE CONTOUR LINES

It is noticed that high conductance contour lines in an open quantum cavity can be closely related to scar states around classical periodic orbits in the corresponding closed system [13, 14]. For the graphene cavity we studied in this work, two types of high conductance contour lines are observed: straight high conductance contour lines and parabolic-like high conductance contour lines. Along a straight high conductance contour line, the wave function probability distribution is found to exhibits nearly the same scarring pattern and is thus closely related to the same classical orbit. Assume that the orbit has length L and net enclosed area S , the action of motion in the presence of a magnetic field is $I = \oint \mathbf{p} \cdot d\mathbf{q} = \hbar \oint \mathbf{k} \cdot d\mathbf{q} + e \oint \mathbf{A} \cdot d\mathbf{q} = \hbar k \cdot L + eBS$. Once there is I_0 with $B = 0$ and $k = k_0$ that satisfies the

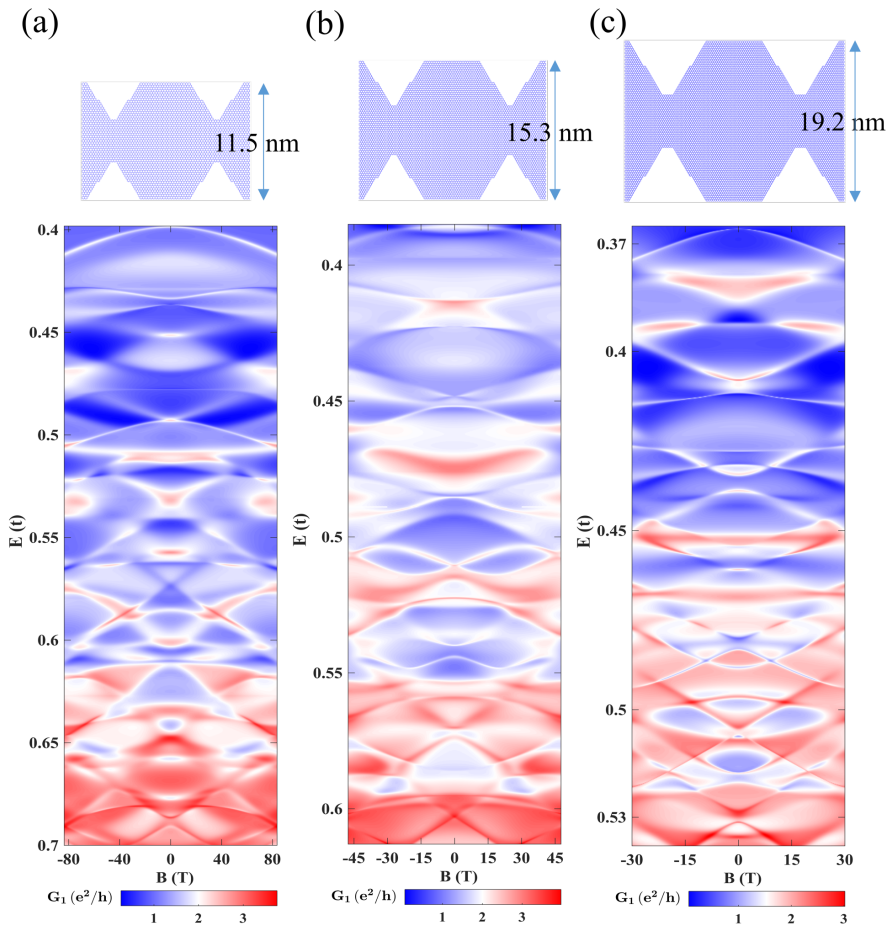


FIG. S3: Conductance maps of three graphene cavity devices, where the cavities have the same shapes but different sizes as indicated in the device model structures displayed in top panels.

Bohr-Sommerfeld quantization rule, i.e., the overall accumulated phase after cycling the orbit is integer multiples of 2π , a scar state around this orbit appears. The scar will persist when varying k and B in such a way that the action of motion is unchanged. Explicitly, this condition can be written as

$$k = k_0 \pm eSB/(\hbar L), \quad (13)$$

where the sign depends on the orientation of the local current circulating the magnetic flux. For graphene, $E = \pm \hbar v_F k$ around the Dirac point. Therefore $E = E_0 \pm (v_F eS/L) \times B$, where the Fermi velocity is given by $v_F = 3ta_0/2\hbar$, i.e., E depends linearly on B .

In a two-dimensional electron gas (2DEG) described by the Schrödinger equation, the dispersion relationship is $E = \hbar^2 k^2/(2m^*)$, where m^* is the effective mass. Therefore, when solving the system with the finite difference method, the system is discretized into a square lattice and, from Eq. (13), we can get $E/t_S = [\sqrt{E_{B=0}/t_S} \pm eBaS/(\hbar L)]^2$, where a is the distance of two nearest-neighbor sites and $t_S = \hbar^2/(2m^* a^2)$ is the hopping energy between two nearest-neighbor sites. Thus, the straight high conductance contour lines observed in our experiments are inherent to the massless

relativistic quantum cavity, as for the Schrödinger case E will depend on B parabolically [15].

However, since typically $E_{B=0}$ is large, this magnetic field dependence in the vicinity of $B = 0$ can be approximated by

$$\frac{E}{t_S} \approx \frac{E_{B=0}}{t_S} \pm 2\sqrt{\frac{E_{B=0}}{t_S} \frac{eaS}{\hbar L}} B.$$

Thus, E also depends on B linearly at small B . However, the slope of a high conductance contour line at $B = 0$ for graphene is $v_F eS/L$, which is a constant. While for the Schrödinger case, it is $2\sqrt{\frac{E_{B=0}}{t_S} \frac{eaS}{\hbar L}}$ and thus a function of energy $E_{B=0}$, which becomes larger as the energy goes higher. To validate the above reasoning, we have calculated the conductance maps for a graphene cavity and a Schrödinger cavity of the same shape. The results are shown in Fig. S4. As guided by the yellow dashed lines, the difference is quite obvious.

For the parabolic-like high conductance contour lines observed in our experiments, as demonstrated by the calculated local current flows, the areas enclosed by the vortices circulating in opposite directions are the same at zero magnetic field and thus the total effective area $S = 0$. However, at a finite

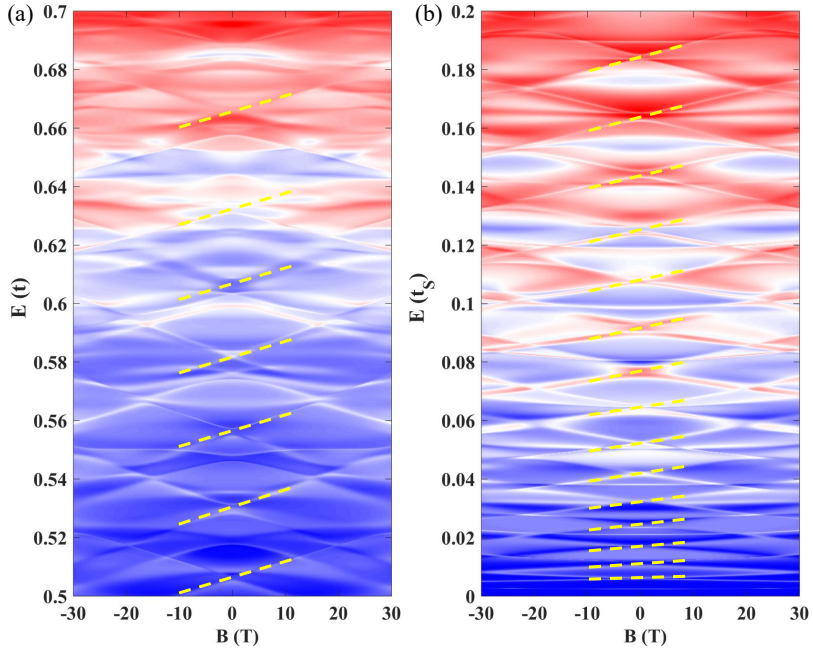


FIG. S4: Comparison between the conductance maps of a graphene and Schrödinger cavity device with the same shaped cavities. Here, the widths of the leads are constructed such that they can support the same maximum number of transmission modes. (a) Conductance map for the graphene cavity with $E \in (0.5t, 0.7t)$ and $B \in (-3.80 \times 10^{-4}B_0, 3.80 \times 10^{-4}B_0)$. (b) Conductance map for the Schrödinger cavity with $E \in (0, 0.2t_s)$ and $B \in (-2.67 \times 10^{-4}B_0, 2.67 \times 10^{-4}B_0)$.

magnetic field, this balance is broken and the difference in the total effective area enclosed by the vortices of opposite directions is no longer zero and is increased with increasing magnetic field B . Based on the above relation between E and B and assuming reasonably that the length L of the orbit changes little with B , it would naturally be expected to parabolic-like high conductance contour lines would also be observed in the the graphene cavity. However, it should be noted that the appearance of a parabolic-like high conductance contour line is common for nonrelativistic quantum system at low magnetic fields. But, here, it arises from a completely different mechanism.

V. EFFECT OF VARIATION IN CAVITY SHAPE

In our simulation, we choose a cavity that is geometricaly similar to the experimental device. As a result, the edges are not perfect, existing certain roughness. To see whether the cavity shape and imperfectness have significant influences, we construct a few graphene cavities of different shapes and compute the conductance maps of these cavities. Figure S5 shows the results of the calculations. It is clear that if the change in cavity shape is small, as for the first three cavities in Fig. S5, the conductance map changes little in characteristics. However, if the shape changes a lot, see Fig. S5(d), clear differences are observable in the calculated conductance map. In addi-

tion, when comparing these calculations to the results shown in Fig. S3, it is seen that boundary imperfectness has a little effect on the main characteristics seen in the conductance map.

VI. EFFECT OF SCATTERERS ON THE CONDUCTANCE MAPS AND SCAR PATTERNS

In the device studied in the main article, the mean free path of carriers is around 100 nm, while the phase coherent length is above 1 μm , i.e., the size of the device. Thus, the system can be regarded as a phase coherent, disordered, mesoscopic system and, on average, there are ~ 100 scatterers in the system. To see whether the scatterers have crucial influence on the results, we have carried out simulations for the cavity device with scatterers included.

For the scatterer, we assume that the scattering at x_i and y_i has a potential of the Gaussian function form [17, 18],

$$U_i(x, y) = U_{i,0} \exp\left(-\left[\frac{(x - x_i)^2}{2\sigma_x^2} + \frac{(y - y_i)^2}{2\sigma_y^2}\right]\right),$$

where i is the index for the scatterer, $|U_{i,0}|$ describes the potential strength, and σ_x and σ_y are the potential localization parameters which we set as the distance between two nearest neighboring atoms. In our calculations, 100 scatterers are distributed randomly in the device with half of them having

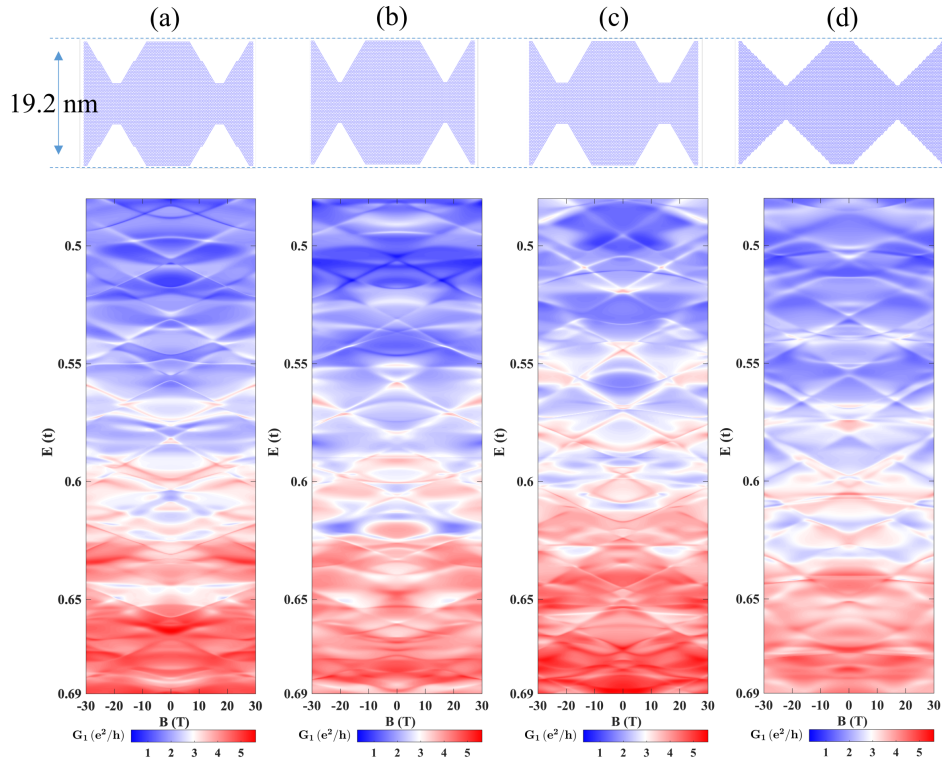


FIG. S5: Conductance maps of four different graphene cavity devices. (a) Conductance map of the graphene cavity device considered for numerical calculations in the main article. Note that the cavity edges are not perfect as we try to mimic the actual shape of the device studied in the experiment. (b) Conductance map of a graphene cavity device with removed cavity edge roughness, where the cavity is slightly wider than the cavity in (a). (c) Conductance map of a cavity device with removed cavity edge roughness, where the cavity is slightly narrower than the cavity in (a). (d) Conductance map of a cavity device with a 45° inclination hypotenuse, where the boundary is a mixture of zigzag and armchair segments. This cavity is very different from the cavities in (a), (b) and (c), where the inclination angle is around 60° and is composed mostly of zigzag edges. The leads have the width of 19.2 nm in all the four devices. All the conductance maps are plotted with the same color scales.

positive values of $U_{i,0}$ and the other half negative values of $U_{i,0}$.

We calculated the conductance map under of the device under different strengths of the scattering potentials. Figures S6(a) to S6(e) show the results of the calculations with the strength $U_{i,0} = 0, \pm 0.1t, \pm 0.2t, \pm 0.3t$ and $\pm 0.5t$, respectively, in the ranges of the energy and magnetic field as in the main article. The top panels in Figs. S6(a) to S6(e) display the assumed distributions and scattering potential profiles. It is clear that when the strength of the scattering potential is small, e.g., in the case of $|U_{i,0}| \leq 0.4t$, the conductance map changes little. However, it is also noticeable that the sharpness of the high conductance contour lines is deteriorated as the strength increases. For example, for $|U_{i,0}| = 0.5t$, the linear high conductance contour line patterns become very much

blurred. However, even in this case, the main conductance contour structures still persist in the map. In addition, we have chosen for each map two points on a high conductance contour line and examine the LDOS and the local current flows at the two points in the presence of scatterers. The results are shown in Fig. S7. It is seen that when $|U_{i,0}| \leq 0.4t$, the effects of the scatterers on the conductance map are negligible. However, when $|U_{i,0}| = 0.5t$, both the LDOS and the local current flows are disturbed significantly.

From the above set of numerical results, it is clear that even if there are scatterers in the device studied experimentally in the main article, insofar as the strengths of these scatters are not too strong, the main transport characteristics of Dirac particles in the device remain nearly unchanged.

-
- [1] P. R. Wallace, Phys. Rev. **71**, 622 (1947).
[2] S. Reich, J. Maultzsch, and C. Thomsen C, Phys. Rev. B **66**, 035412 (2002).
[3] A. Kretinin, G. L. Yu, R. Jalil, Y. Cao, F. Withers, A. Mishchenko, M. I. Katsnelson, K. S. Novoselov, A. K. Geim, and F. Guinea, Phys. Rev. B **88**, 165427 (2013).
[4] D. K. Ferry, L. Huang, R. Yang, Y.-C. Lai, and R. Akis, J. Phys.: Conf. Ser. 220, 012015 (2010).

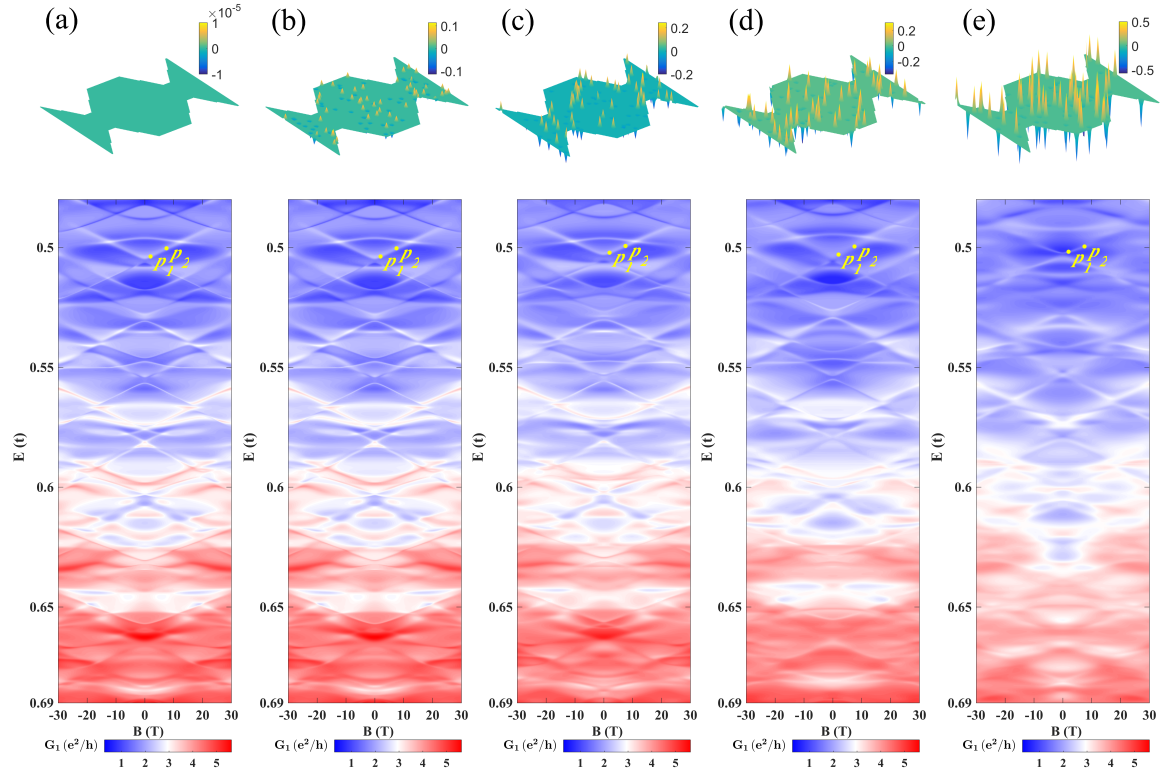


FIG. S6: Conductance maps of a graphene cavity device (a) without scatterers and (b), (c), (d), and (e) with scatters included in the cavity region. The amplitudes of the scatters in (b), (c), (d), and (e) are $\pm 0.1t$, $\pm 0.2t$, $\pm 0.3t$ and $\pm 0.5t$, respectively. The distributions and potential profiles of the scatterers are displayed in top panels. All the conductance maps have the same colorbars. The points marked in each conductance map indicate the parameter values at which the LDOS patterns and local current flow patterns shown in Fig. S7 are calculated.

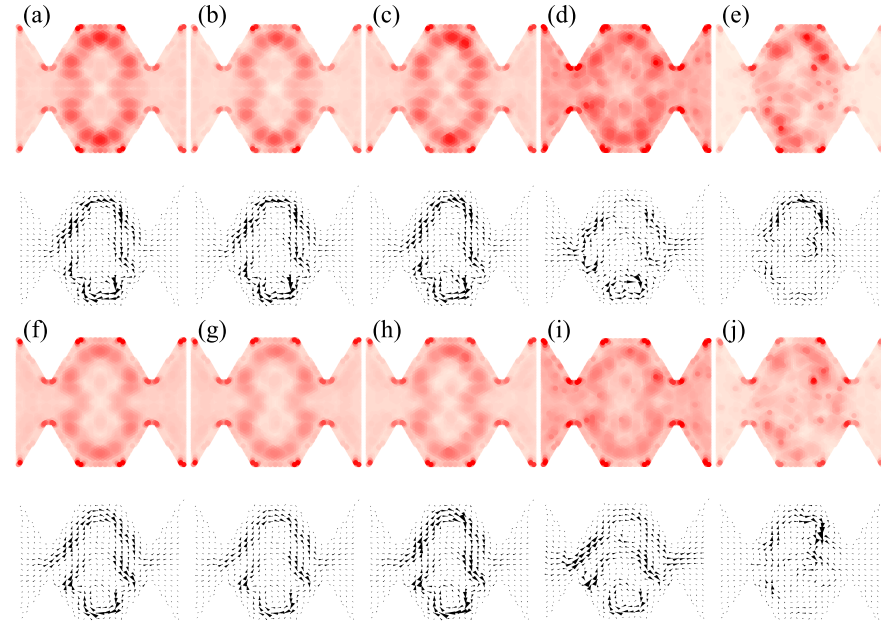


FIG. S7: LDOS and local current density distribution calculated for the same devices as in Fig. S6 at points marked by p_1 ($B = 2$ T, top two rows) and p_2 ($B = 7.5$ T, bottom two rows). The results shown in columns from left to right are for devices in (a) to (e) in Fig. S6.

- [5] A. H. Castro Neto, F. Guinea, N. M. R. Peres, K. S. Novoselov, and A. K. Geim, Rev. Mod. Phys. **81**, 109 (2009).
- [6] R. Landauer, Phil. Mag. **21**, 863 (1970).
- [7] F. Muñoz-Rojas, D. Jacob, J. Fernández-Rossier, and J. J. Palacios, Phys. Rev. B **74**, 195417 (2006).
- [8] T. C. Li and S.-P. Lu, Phys. Rev. B **77**, 085408 (2008).
- [9] L. Huang, Y.-C. Lai, and C. Grebogi, Chaos **21**, 013102 (2011).
- [10] L. Huang, Y.-C. Lai, D. K. Ferry, R. Akis, and S. M. Goodnick, J. Phys.: Condens. Matter **21**, 344203 (2009).
- [11] M. P. Sancho López, J. M. Sancho López, and J. Rubio, J. Phys. F: Met. Phys. **44**, 1205-1215 (1984).
- [12] S. Datta, *Electronic Transport in Mesoscopic Systems* (Cambridge University Press, Cambridge, England, 1995).
- [13] D. K. Ferry, R. Akis, and J. P. Bird, Phys. Rev. Lett. **93**, 026803 (2004).
- [14] L. Huang, Y.-C. Lai, H.-G. Luo, and C. Grebogi, AIP Adv. **5**, 017137 (2015).
- [15] J. P. Bird, R. Akis, D. K. Ferry, A. P. S. de Moura, Y.-C. Lai, and K. M. Indlekofer, Rep. Prog. Phys. **66**, 583-632 (2003).
- [16] L. Ying, L. Huang, Y.-C. Lai, and C. Grebogi, Phys. Rev. B **85**, 245448 (2012).
- [17] J. Xue, J. Sanchez-Yamagishi, D. Bulmash, P. Jacquod, A. Deshpande, K. Watanabe, T. Taniguchi, P. Jarillo-Herrero, and B. J. LeRoy, Nat. Mat. **10**, 282 (2011).
- [18] J. Keski-Rahkonen and P. J. J. Luukko and S. Åberg and E. Räsänen, J. Phys: Condens. Matter **31** 105301 (2019).